Detecting and Characterizing Ekman Currents in the Southern Ocean

CHRISTOPHER J. ROACH

Geophysical Fluid Dynamics Institute, Florida State University, Tallahassee, Florida

HELEN E. PHILLIPS

Institute for Marine and Antarctic Studies, University of Tasmania, and ARC Centre of Excellence in Climate Systems Science, Hobart, Tasmania, Australia

NATHANIEL L. BINDOFF

Institute for Marine and Antarctic Studies, University of Tasmania, and Antarctic Climate Ecosystems Cooperative Research Centre, and ARC Centre of Excellence in Climate Systems Science, and CSIRO Marine and Atmospheric Research, Hobart, Tasmania, Australia

STEPHEN R. RINTOUL

Antarctic Climate Ecosystems Cooperative Research Centre, University of Tasmania, and CSIRO Marine and Atmospheric Research, Hobart, Tasmania, Australia

(Manuscript received 18 June 2014, in final form 6 January 2015)

ABSTRACT

This study presents a unique array of velocity profiles from Electromagnetic Autonomous Profiling Explorer (EM-APEX) profiling floats in the Antarctic Circumpolar Current (ACC) north of Kerguelen. The authors use these profiles to examine the nature of Ekman spirals, formed by the action of the wind on the ocean's surface, in light of Ekman's classical linear theory and more recent enhancements. Vertical decay scales of the Ekman spirals were estimated independently from current amplitude and rotation. Assuming a vertically uniform geostrophic current, decay scales from the Ekman current heading were twice as large as those from the current speed decay, indicating a compressed spiral, consistent with prior observations and violating the classical theory. However, if geostrophic shear is accurately removed, the observed Ekman spiral is as predicted by classical theory and decay scales estimated from amplitude decay and rotation converge toward a common value. No statistically robust relationship is found between stratification and Ekman decay scales. The results indicate that compressed spirals observed in the Southern Ocean arise from aliasing of depth-varying geostrophic currents into the Ekman spiral, as opposed to surface trapping of Ekman currents associated with stratification, and extends the geographical area of similar results from Drake Passage (Polton et al. 2013). Accounting for this effect, the authors find that constant viscosity Ekman models offer a reasonable description of momentum mixing into the upper ocean in the ACC north of Kerguelen. These results demonstrate the effectiveness of a new method and provide additional evidence that the same processes are active for the entire Southern Ocean.

1. Introduction

V. W. Ekman's theory of wind forcing on the surface ocean is a cornerstone of oceanography (Ekman 1905). By considering a balance between frictional and Coriolis forces and assuming momentum mixing parameterized by a constant vertical eddy viscosity k, Ekman (1905) derived an equation for the latitudinal and longitudinal velocity components as a function of depth:

$$\text{if} \quad \mathbf{U}_{\text{ek}} = \frac{1}{\rho}\frac{\partial \boldsymbol{\tau}(z)}{\partial z} = k\frac{\partial \mathbf{U}_{\text{ek}}}{\partial z}, \tag{1}$$

where $\mathbf{U}_{\text{ek}}$ denotes the Ekman velocity in the form $u_{\text{ek}} + iv_{\text{ek}}$, and $\boldsymbol{\tau}(z)$ denotes the turbulent stress.

For steady winds, the resulting solution is the Ekman spiral, which has a characteristic exponential amplitude

Corresponding author address: Christopher Roach, Geophysical Fluid Dynamics Institute, 018 Keen Building, Florida State University, Tallahassee, FL 32306-4360.
E-mail: croach@fsu.edu

DOI: 10.1175/JPO-D-14-0115.1

decay and anticyclonic (anticlockwise in the Southern Hemisphere) rotation with increasing depth.

Integrating flow over the depth of the Ekman spiral results in a net transport that is 90° to the left of the wind in the Southern Hemisphere. Ekman transport is central to the wind-driven circulation and within the Southern Ocean is significant in the meridional overturning circulation, driving the upwelling of deep waters near 50°S (Speer et al. 2000) and transporting them northward. It is also significant in the formation of mode waters (Sallée et al. 2006).

Previous studies using direct observations of upper-ocean velocity have established the validity of the bulk relationship between wind stress and net Ekman transport (Chereskin 1995; Chereskin and Roemmich 1991; Halpern 1974; Price et al. 1987). Other studies have also found Ekman-like spirals in data averaged over long time periods (Chereskin 1995; Hunkins 1966; Lenn and Chereskin 2009; Price et al. 1987).

These studies found the classical constant viscosity model inadequate. Time-mean spirals were "compressed"; the current amplitude decayed more quickly with depth than predicted by classical theory. It has been suggested this compression is a result of stratification-driven surface trapping (Price and Sundermeyer 1999; Price et al. 1987). However, two recent studies, one employing spectral methods (Elipot and Gille 2009) and a second considering the effect of depth-varying geostrophic currents (Polton et al. 2013), suggest it is possible to reconcile observed Ekman currents to the constant viscosity Ekman model.

In this paper, we present approximately 1400 high-resolution, concurrent temperature salinity and horizontal velocity profiles. These profiles were collected with eight Electromagnetic Autonomous Profiling Explorer (EM-APEX) velocity profiling floats (Sanford et al. 2005) deployed north of Kerguelen Island in the Antarctic Circumpolar Current (ACC) standing meander during the 2008 Southern Ocean Finestructure (SOFINE) expedition (Naveira Garabato et al. 2009; Phillips and Bindoff 2014). The data present a unique view of the upper ocean as the floats are advected with the ACC. The vertical resolution of profiles, approximately 3-dbar spacing, is much finer than for ADCP velocities commonly used to investigate the Ekman layer (e.g., Lenn and Chereskin 2009). The profiles are closely spaced along trajectories and the temporal sampling resolves the inertial frequency. The density of profiles obtained allows us to investigate Ekman currents without averaging over long time periods as in some earlier work (e.g., Lenn and Chereskin 2009; Elipot and Gille 2009). We use this dataset to isolate and describe Ekman currents and to investigate the possibility of reconciling observed Ekman currents to time-mean classical Ekman theory in a new location in the Southern Ocean. Further, we extend previous studies to specifically examine the role of stratification in these water masses on surface Ekman currents.

The primary result of this study agrees with earlier work by Polton et al. (2013) in the Drake Passage, which demonstrates that within the Southern Ocean context of deep and weakly stratified mixed layers, compression of Ekman spirals is due to aliasing of depth-varying geostrophic currents into the Ekman spiral. This result says that a constant eddy viscosity adequately represents the vertical structure of the Ekman current. Furthermore, eddy viscosity profiles computed from the relationship between turbulent stress and shear are consistent with eddy viscosity predicted from classical linear theory. We also found that stratification had no significant influence on Ekman current decay scales in this region of the Southern Ocean.

The datasets and methodology used in this study are discussed in sections 2 and 3. In section 4, we identify and characterize the observed Ekman currents, which are then used to calculate the net Ekman transport in section 5. Potential relationships between Ekman currents and stratification are explored in section 6.

2. Datasets

a. *EM-APEX float data*

EM-APEX floats (Sanford et al. 2005) are a development of the APEX subsurface profiling float manufactured by Teledyne–Webb, which makes up much of the current Argo fleet. In addition to the standard CTD system of Argo floats, EM-APEX floats are equipped with an electromagnetic subsystem that measures the motion-induced electric fields generated by currents moving through the vertical component of Earth's magnetic field. Two orthogonal pairs of electrodes give independent measurements of electrical potential difference across the body of the float. As the instrument ascends/descends at 10–12 cm s^{-1}, external fins cause the body to rotate so that the orientation of the electrode axes relative to the instantaneous current is constantly changing. Onboard processing performs a least squares fit (LS) over a moving window of 50-s duration to give voltage component pairs at a vertical resolution of 2–4 dbar. The electric field measurements are converted to relative velocity components following the method described in Sanford et al. (1978). The unknown constant velocity offset is determined from the GPS locations at each surfacing of the float, as described in Phillips and Bindoff (2014), allowing absolute velocities to be calculated.

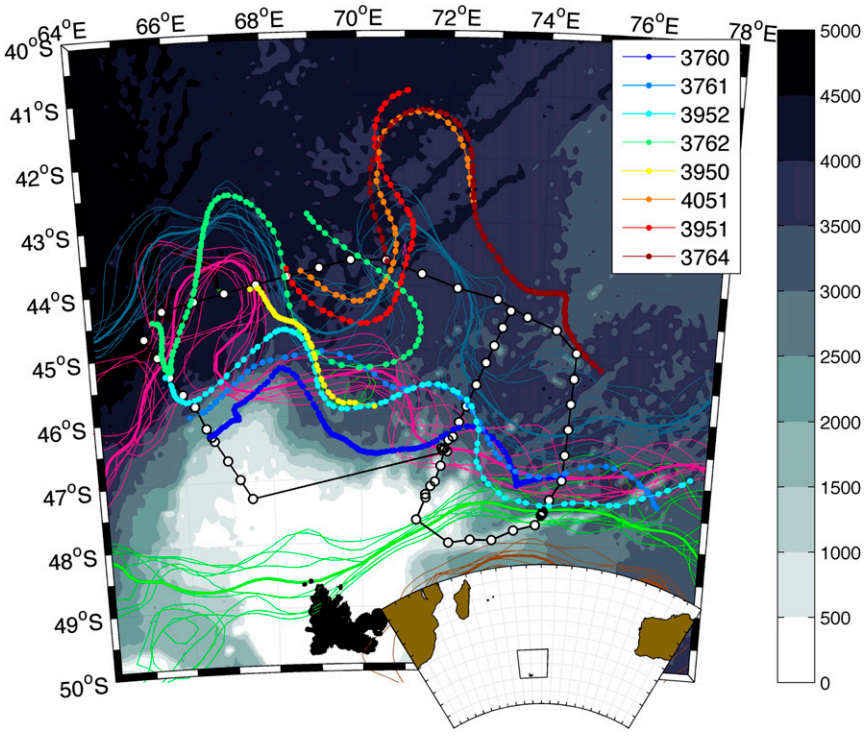

FIG. 1. Location of profiles from eight EM-APEX floats (colored circles) and SOFINE cruise track and CTD locations (white circles). Background shading (m) is Smith and Sandwell (1997) bathymetry. Colored contours from north to south mark the location of the northern (gray), central (pink), and southern (green) branches of the Subantarctic Front and the northern Polar Front (brown) based on sea surface height (SSH) labels. Weekly and mean front positions (fine and heavy lines, respectively) are shown for AVISO SSH anomalies over the period 18 Nov 2008–14 Jan 2009 added to mean dynamic height of 100 dbar relative to 2500 dbar.

The data used in this study were collected using eight EM-APEX floats deployed north of Kerguelen Island in November 2008 during the SOFINE expedition (Fig. 1). The floats returned over 1400 profiles with samples spaced approximately 3 m in the vertical. The horizontal separation of profiles was 2–10 km, depending on the mean currents. Within the Kerguelen Island region, all floats took four profiles (two descent–ascent cycles) per day. Once downstream of Kerguelen Island, floats were reprogrammed to produce ''bursts'' of four profiles a day with each burst separated by 9 days, consistent with Argo program sampling.

During this study the latitude of the EM-APEX floats ranged from 41° to 49°S, with inertial periods between 15.9 and 18.2 h. The profiling mission was designed to ensure that, while the floats were near Kerguelen Island, pairs of adjacent upcasts or downcasts were separated by approximately half an inertial period. Example absolute velocity, temperature, and salinity profiles are shown in Fig. 2. This profiling pattern allows the isolation and removal of velocities arising from inertial oscillations following a method described in Phillips and Bindoff (2014). Calibration and quality control of the velocity data are described in Phillips and Bindoff (2014). Quality control of the temperature and salinity dataset is described in Meyer et al. (2015).

b. *Wind data*

To examine the wind forcing within the Kerguelen region we used gridded wind fields (Bentamy et al. 2009) produced by the Institut Francais de Recherche pourl'Exploitation de la Mer (IFREMER), Department of Oceanography, and the Centre ERS d'Archivage et de Traitement (CERSAT). This dataset was produced by merging QuickSCAT scatterometer winds with SSM/I radiometer wind speeds and ECMWF reanalysis wind fields using an objective method (Bentamy et al. 2009). The resulting 10-m wind fields offer 0.25° spatial resolution and 6-h temporal resolution.

Wind velocities from the blended wind fields were interpolated onto the time and location of each EM-APEX profile and then converted to wind stresses using drag coefficient functions from Yelland and Taylor (1996). Time series of wind stress are shown in Fig. 3 for floats

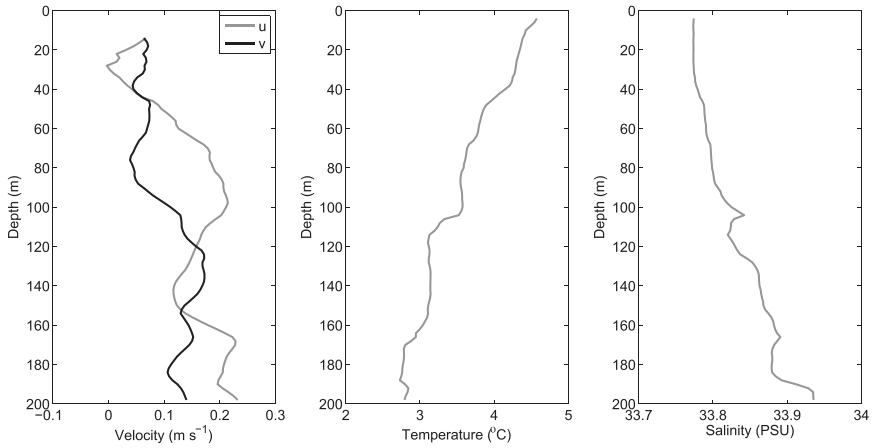

FIG. 2. Example of measured velocity components (left) u eastward and v northward, (middle) in situ temperature, and (right) salinity profiles obtained by EM-APEX float 3760.

3760, 3762, and 3764 at the southern, central, and northern limits of the survey, respectively. Winds were generally low, with meridional wind stresses typically less than 0.2 Pa and zonal wind stresses close to 0 Pa. These low winds were interrupted by a number of short duration, high-amplitude events. The resulting time-mean wind stress was directed to the east with an amplitude of 0.099 Pa.

c. *TPXO7.2 tides*

To investigate the potential for tidal signals to affect our observations we used the TOPEX/Poseidon (TPXO7.2) barotropic tide inverse model with global 0.25° spatial resolution. Details of the model are given in Egbert and Erofeeva (2002). The model was evaluated to determine tidal velocities at the times and locations of all EM-APEX float profiles.

d. *Wave data*

Some statistical information about the surface wave field is contained in the raw EM-APEX electrical potential measurements (Sanford et al. 2011; Sanford et al. 2005). However, our lack of sufficient reliable observations between the surface and 14 m prevented such an analysis. Hence, mean wave period, significant wave height, and mean wave heading were sourced from the

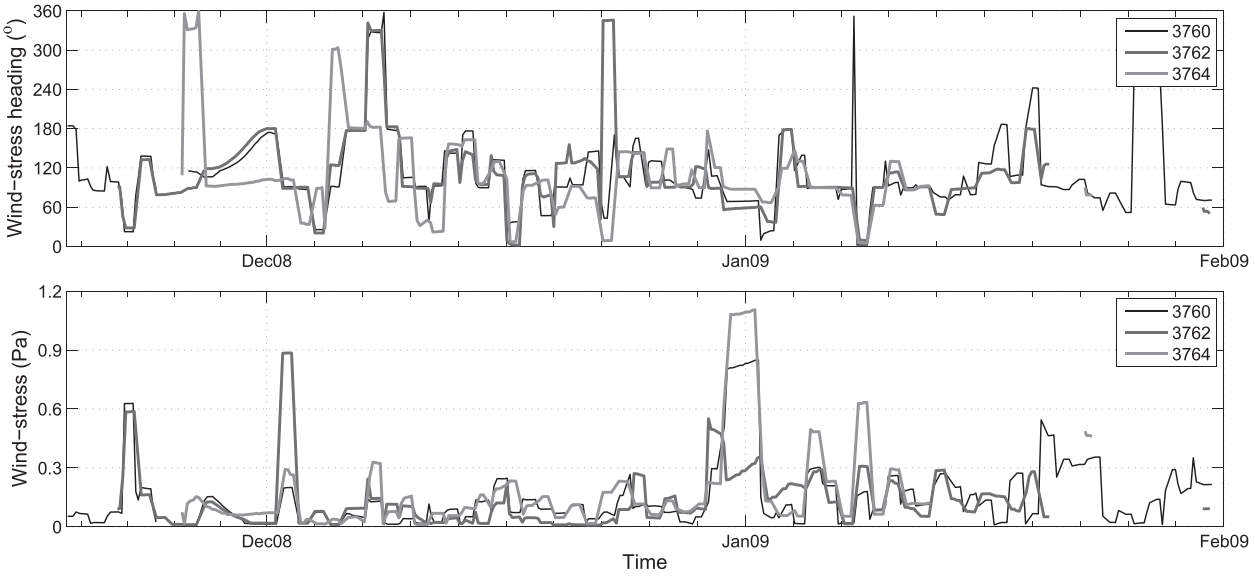

FIG. 3. (top) Wind stress heading (positive clockwise from north) and (bottom) amplitude for floats 3760, 3762, and 3764, representing winds at the south, middle, and north of the study domain, respectively, from IFREMER-blended satellite reanalysis winds.

ECMWF's ERA-Interim reanalysis dataset (Persson and Grazzini 2007). This dataset is derived from an atmospheric model coupled to a WAM-type ocean wave model (Hasselmann et al. 1988), driven by data assimilated from a variety of sources. The resulting dataset has a 0.25° spatial resolution and a 6-h temporal resolution.

3. Method

a. Isolating Ekman currents

Ekman currents constitute an ageostrophic flow field resulting from the dynamical balance involving the wind stress and Coriolis force. Before we can examine Ekman currents, the geostrophic component of velocity (often larger than the Ekman flow) must be removed. An obvious approach would be to calculate geostrophic velocities from the hydrographic data collected by the floats using the thermal wind equations. In practice, this is impractical as the EM-APEX floats tend to follow streamlines, so that using the thermal wind equations would only resolve the weak cross streamflow. Hence, we tested two alternative approaches for estimating the geostrophic flow.

1) NO SHEAR CASE

First, in line with a number of previous studies (Chereskin 1995; Lenn and Chereskin 2009), we assumed geostrophic shear was negligible within the upper ocean and so defined the subinertial currents in the Ekman layer to be the sum of the depth-varying Ekman currents $\mathbf{U}_{\rm ek}$ and a constant geostrophic reference velocity $\mathbf{U}_{\rm deep}$:

$$\mathbf{U}_M(z) = \mathbf{U}_{\rm ek}(z) + \mathbf{U}_{\rm deep}. \tag{2}$$

The current $\mathbf{U}_{\rm ek}(z) = u_{\rm ek} + iv_{\rm ek}$ was assumed to follow the solution associated with a classical Ekman spiral with components $u_{\rm ek}$ (east) and $v_{\rm ek}$ (north) defined as

$$u_{\rm ek} = V_0 e^{z/|D_e|} \cos\left(\frac{-z}{D_e} + \theta_0 + \frac{\pi}{4}\right), \quad \text{and} \tag{3a}$$

$$v_{\rm ek} = V_0 e^{z/|D_e|} \sin\left(\frac{-z}{D_e} + \theta_0 + \frac{\pi}{4}\right), \tag{3b}$$

where the depth z is taken as positive upward, V_0 denotes the surface current speed, and θ_0 denotes the wind stress heading (here in radians). The term D_e denotes the Ekman decay scale, with positive values corresponding to anticlockwise rotation (as expected from Ekman theory) and negative values corresponding to reversed rotation. The value $\mathbf{U}_{\rm deep}$ is chosen to be the velocity at a level below which the Ekman component should be negligible.

During their study within the Drake Passage, Lenn and Chereskin (2009) used a reference velocity at a depth of 98 m based on ADCP measurements of shear from multiple voyages over a period of 7 yr. We do not have such a long record of the vertical shear in the Kerguelen region independent of the EM-APEX data. Instead, we used the 200-m level velocity time series as the reference velocity. This places our reference velocity below the expected mixed layer depth (MLD) range for the Kerguelen region of 100–200 m (Sallée et al. 2006). For the rest of this paper we denote this method of defining the geostrophic velocity as the "no shear" case.

For each profile, two Nelder–Mead (NM) simplex searches (Nelder and Mead 1965) were run to search for the parameters V_0, θ_0, and D_e that minimized the cost function L:

$$L = \sum_{z=-50\text{m}}^{z=0\text{m}} |\mathbf{U}(z) - \mathbf{U}_M(z)|.$$

The first set of solutions with the Nelder–Mead algorithm assumed an Ekman component with anticlockwise rotation (as expected in the Southern Hemisphere), and the other solution assumed an Ekman component with clockwise rotation. Note the solution of this system of equations is intrinsically nonlinear since the surface current speed, current heading, and Ekman decay scale appear inside the terms on the right side of Eqs. (3a) and (3b). Initial inputs for both the simplex searches were taken to be an Ekman decay scale of 20 m, a surface velocity with speed equal to the uppermost ocean velocity observation, and heading in the direction of the wind stress.

2) SHEAR CASE

The assumption of a constant geostrophic velocity within the mixed layer is not supported by observations undertaken during SOFINE (Phillips and Bindoff 2014). In these observations, the Antarctic Circumpolar Current was found to display strong depth-varying flow (Fig. 2). In line with the large-scale dynamics of the Southern Ocean, geostrophic flow and mean wind displayed similar mean headings. It is therefore possible that depth-varying geostrophic flow is aliased into the Ekman velocity in the no shear case. Recent results in the Drake Passage region (Polton et al. 2013) also show that failure to account for geostrophic shear in the Ekman layer results in compressed spirals. We considered two methods to remove geostrophic shear (henceforth denoted as shear 1 and shear 2 cases) in which we assumed the complex near-surface subinertial currents $\mathbf{U}_M$ could be described as the sum of an Ekman component $\mathbf{U}_{\rm ek}$, a constant reference velocity $\mathbf{U}_{\rm deep}$, and a component arising from a constant geostrophic shear:

$$\mathbf{U}_M(z) = \mathbf{U}_{\rm ek}(z) + \mathbf{U}_{\rm deep} + \frac{d\mathbf{U}_{\rm geo}}{dz} z. \tag{4}$$

In line with the no shear case, two Nelder–Mead simplex searches were run to fit parameters V_0, θ_0, D_e, and the linear shear (i.e., $d\mathbf{U}_{\text{geo}}/dz$ is constant) across the Ekman layer. Initial inputs for V_0, θ_0, and D_e were the same as for the no shear case, while the linear geostrophic shear was estimated as the shear between 100- and 200-m depth. For shear 1, we assumed the Ekman current consisted of a classical spiral and hence took the solutions generated by the Nelder–Mead fit initialized assuming anticlockwise (anticyclonic) rotation. For the shear 2 case, we considered the possibility of the Ekman component displaying reversed rotation as seen in frequency domain solutions of the Ekman equations (Elipot and Gille 2009) and initialized with clockwise rotation. Hence, for each profile we considered Nelder–Mead fits initialized with both clockwise and anticlockwise rotation and took the solution from whichever one of the two displayed the minimal residual. It is worthwhile noting that regardless of the assumed starting conditions both the shear 1 and shear 2 Nelder–Mead fits can produce both Ekman-like and reversed spirals (Table 1).

While the assumption of constant geostrophic shear is the same as in Polton et al. (2013), our method differs in both the use of a simplex search to apply fits and by including the geostrophic shear in the optimization problem instead of first removing it. It also extends the region of validity; the Drake Passage is a different region, with a more constrained flow relative to the Kerguelen Plateau region.

The observed Ekman current profiles were rotated into a wind-relative reference frame using wind estimates from the IFREMER-blended reanalysis–scatterometer wind fields (Bentamy et al. 2009) and mapped onto a regular 2-m depth grid before averaging to produce time-mean hodographs of velocity. This suppresses variability arising from variations in wind heading and allows these results to be compared with prior studies (Lenn and Chereskin 2009; Price et al. 1987; Schudlich and Price 1998).

b. *Evaluating performance of fits and estimating eddy viscosities*

The classical Ekman spiral can be separated into a velocity amplitude component decaying exponentially with increasing depth $|\mathbf{U}_{\text{ek}}(z)|$ and a unit vector component with a heading $\theta(z)$, rotating anticlockwise as a linear function of increasing depth:

$$|\mathbf{U}_{\text{ek}}(z)| = V_0 e^{z/|D_e|}, \quad \text{and} \tag{5a}$$

$$\theta(z) = z/D_e. \tag{5b}$$

The fraction of variance R^2 values in each observed profile of current speed and heading captured by the NM fits of Eqs. (5a) and (5b) were calculated. If the R^2 for the fit to current amplitude exceeded 0.75, the rotational R^2 exceeded 0.5, and the decay scale D_e was less than 500 m, the profile was classified as displaying a spiral and the direction of rotation was obtained. Eddy viscosities k were then calculated from estimated Ekman layer depths, and the Coriolis parameter f was calculated as

$$k = \frac{D_e^2|f|}{2}. \tag{6}$$

Finally, we generated Ekman spirals for all profiles from the fitted Ekman decay scales using the solutions for the ''classical'' case, which assumes constant wind forcing and constant density in the upper ocean. These estimated velocity profiles [$\mathbf{U}_M(z)$; Eq. (4)] were subtracted from the corresponding observed velocities to obtain residuals that were then used to assess the performance of the fitting procedures (see section 4a).

Ekman decay depth and eddy viscosity are obtained from the Nelder–Mead fitting procedure outlined above. However, in line with previous studies (Chereskin 1995; Lenn and Chereskin 2009), we also obtained estimates of Ekman depth based on the rate of rotation with depth of the horizontal velocity vector and on the rate of velocity amplitude decay observed in each individual spiral. Equations (5a) and (5b) were fitted independently of each other to the upper 50 m of each velocity profile using a least squares technique. These fits produced two estimates of decay scale D_e, which we denote D_{amp} from the amplitude fit [Eq. (5a)] and D_{rot} from the rotational fit [Eq. (5b)]. The fitted velocity profiles were then classified as Ekman spirals, reversed spirals, or neither, and the decay scales and viscosity were recorded for each, as was done for the NM fits in section 3a.

The 95% confidence intervals (CI) on decay scales and viscosities were calculated as

$$\text{CI} = \overline{x} \pm \frac{1.96\sigma}{\sqrt{n}}, \tag{7}$$

TABLE 1. Number of Ekman-like spirals and reversed spirals detected in observed velocity profiles with either linear geostrophic shear (shear 1 and shear 2) or no shear assumed over the Ekman layer and using either the NM simplex search described in section 3a or the LS described in section 3b. Shear 1 (shear 2) is where fits are initialized with anticlockwise (clockwise) rotation.

	Number of spirals	
	Ekman	Reverse
NM shear 1	441	39
NM shear 2	313	227
NM no shear	224	150
LS shear 1	445	109
LS shear 2	359	236
LS no shear	249	186

where $\bar{x}$ denotes the mean value, σ denotes the standard deviation, and n denotes the number of degrees of freedom. Here, we assumed one degree of freedom per profile.

c. Calculating transport

Each observed Ekman velocity profile was rotated into a wind-relative coordinate system defined by the wind vector at the time and place of each profile to give $u_e + iv_e$. Volume transport per unit pathlength T was then calculated by integrating observed velocities upward from 200 m to the surface:

$$T(z) = \int_{-200\text{m}}^{0\text{m}} (u_e + iv_e)\, dz. \tag{8}$$

We tested the sensitivity of net transport computed from the EM-APEX data to the choice of integration depth between 100 and 200 m (not shown) and determined that its impacts were not statistically significant.

Because of the time needed for an EM-APEX float to "spin up" at the start of its descent, velocity observations are sparse between the 14-m depth level and the surface. For example, at 8-m depth less than half the profiles have a valid velocity observation. To correct for this, and allow us to compute transport to the surface, we confined our examination of transport to 1335 profiles with velocity observations at or above 14 m. We extrapolated these current profiles to the surface assuming a slab layer (i.e., constant velocity layer) between the shallowest observation and the surface (Lenn and Chereskin 2009). The mean wind-relative transport was then calculated by averaging all these transport estimates.

The observed near-surface transport was then compared with estimates calculated from reanalysis winds using the well-established relationship (e.g., Chereskin 1995)

$$T_x = \frac{\tau_y}{f\rho}, \quad T_y = \frac{-\tau_x}{f\rho}, \tag{9}$$

where τ_x and τ_y denote eastward and northward components of surface wind stress, and ρ denotes density.

When computing 95% confidence intervals on transport we used Eq. (7) and assumed one degree of freedom per two profiles (approximately one degree of freedom per 12 h). This time scale of 12 h represents our understanding of the oceanographic noise and is shorter than the dominant time period of weather systems of a few days and thus allows the weather-driven changes in the ocean to be observed. We did not consider additional degrees of freedom introduced by other factors (e.g., Stokes drift). Consequently, error bars in later sections may be conservative.

While the total Ekman transport has been shown to be well represented by classical theory (Chereskin 1995; Chereskin and Roemmich 1991; Price et al. 1987; Wijffels et al. 1994), the vertical structure of this transport is still under debate. Several studies have suggested that transport within the mixed layer can best be described with a slablike model (Halpern 1974; Wijffels et al. 1994), that is, vertically uniform transport within the mixed layer with little transport occurring deeper in the water column. Other studies (e.g., Chereskin and Roemmich 1991) have detected transport profiles displaying significant variability with depth, inconsistent with a slablike model. To investigate this, we mapped mean Ekman velocities and transport onto a vertical coordinate defined as observation depth divided by MLD. MLD was calculated from each EM-APEX density profile using a density criterion of $\Delta\sigma < 0.03\,\text{kg m}^{-3}$ relative to the uppermost observation (Sallée et al. 2006). MLD in our observations ranged from 7 to 330 m, with a mean of 43.8 m and a standard deviation of 25.2 m.

d. Local estimates of eddy viscosity

The classical, steady-state Ekman solution (Ekman 1905) is a balance between turbulent stress and vertical shear. Equation (1) can be rearranged to give viscosity in terms of stress, Ekman shear, and density (e.g., Chereskin 1995; Lenn and Chereskin 2009):

$$k(z) = \frac{\boldsymbol{\tau}(z)}{\rho} \frac{1}{(\partial \mathbf{U}_{\text{ek}}/\partial z)}. \tag{10}$$

The stress profile can be estimated by integrating $\mathbf{U}_{\text{ek}}$ upward from a deep reference level (h_e):

$$\boldsymbol{\tau}(z) = i\rho f \int_{h_e}^{z_i} \mathbf{U}_{\text{ek}}\, dz. \tag{11}$$

Stress, shear, and viscosity profiles were calculated from Eqs. (10) and (11) for each profile and then a mean viscosity profile was computed over all data. As in the preceding analysis of transport, the resulting profiles of stress, shear, and viscosity were remapped onto the MLD coordinate prior to averaging.

4. Observed Ekman spirals

a. Performance of fitting procedures

The number of Ekman spirals detected by each fitting procedure is given in Table 1; RMS residuals between observations and fitted spirals for the 14-m depth level are given in Table 2. In addition to Ekman-like spirals, we identified spirals that passed the classification procedure but displayed reversed rotation. Previous studies (Elipot and Gille 2009; Rudnick and Weller 1993) show reversed spirals are consistent with the time-varying

TABLE 2. Estimates of mean decay scales D_e, eddy viscosities k, and RMS residuals using the different methods outlined in sections 3a and 3b. No shear and shear estimates come from Eq. (5a) for amplitude and Eq. (5b) for rotation. The results labeled Ekman spirals is from the analysis based entirely on profiles that fit the definition of an Ekman spiral (see text). All data refer to the analysis where all velocity profiles with decay scales of less than 1000 m are used, including those that do not meet the definition of a spiral and including reverse spirals. The 95% confidence intervals on decay scales were estimated using Eq. (9). Errors in viscosity were estimated by propagating the uncertainty in D_e through Eq. (6). RMS residuals were computed between observations and fitted spirals at 14-m depth. Shear 1, shear 2, and no shear cases are as defined in Table 1 and section 3.

	No shear				Shear 1				Shear 2			
	D_e (m)	k (10^{-2} m^2 s^{-1})	Number	RMS residual (m s^{-1})	D_e (m)	k (10^{-2} m^2 s^{-1})	Number	RMS residual (m s^{-1})	D_e (m)	k (10^{-2} m^2 s^{-1})	Number	RMS residual (m s^{-1})
Ekman spirals												
Rotational fit	42.59 ± 5.36	9.35 ± 2.35	249	0.1376	40.18 ± 4.61	8.33 ± 1.91	455	0.1343	39.01 ± 5.31	7.85 ± 2.13	359	0.1265
Amplitude fit	25.1 ± 2.66	3.25 ± 0.69	249	0.0816	31.07 ± 3.34	4.98 ± 1.07	455	0.1026	31.40 ± 5.31	5.09 ± 1.72	359	0.0691
NM fit	67.74 ± 15.67	22.92 ± 10.76	224	0.1171	38.53 ± 4.59	7.65 ± 1.82	441	0.0673	34.25 ± 4.61	6.04 ± 1.63	313	0.0557
All Data												
Rotational fit	93.06 ± 9.70	44.71 ± 9.32	1091	0.1179	70.43 ± 7.77	25.61 ± 5.66	1217	0.1155	75.19 ± 8.27	29.20 ± 6.43	1220	0.1147
Amplitude fit	63.36 ± 6.12	20.73 ± 4.01	1091	0.1467	60.63 ± 5.78	18.98 ± 3.62	1217	0.1319	67.83 ± 8.27	23.77 ± 5.80	1220	0.1381
NM Fit	88.75 ± 8.64	40.7 ± 7.93	1397	0.0958	47.24 ± 3.97	13.38 ± 2.09	1397	0.0624	58.5 ± 4.87	17.69 ± 4.76	1397	0.0516

solution to the Ekman balance and suggest that the reversed spirals observed here are plausibly caused by cyclonic rotations of the wind at frequencies higher than the inertial frequencies. Figure 3 shows that there are many periods of cyclonic wind fields, and the more detailed analysis of the relationship between reverse spirals and the in situ wind fields is in Roach et al. (2015, manuscript submitted to *J. Phys. Oceanogr.*). A close analysis of the power spectrum (not shown) of the in situ winds shows that the power is a factor of 3–5 higher than the IFREMER winds at or near the inertial period likely to be providing energy to drive reverse spirals. This indicates it may be necessary to resolve the full time-varying dynamics of Ekman flow. Example hodographs (the projection of the current profile onto the horizontal plane) of both anticlockwise and clockwise spirals are shown in Fig. 4.

We also considered the time-mean current hodograph averaged, in a wind-relative reference frame, over all profiles (Fig. 5, top row) and the profiles identified as displaying Ekman spiral–like behavior using the methodology described in section 3b (Fig. 5, bottom row). All of the time-averaged hodographs display clear anticlockwise rotation and amplitude decay with increasing depth. However, all hodographs placed the shallowest velocity vectors farther downwind than is expected for the classical Ekman case (45° to the left of the wind vector).

Of all fits that generated a valid decay scale (here taken as less than 1000 m), the NM simplex fits (section 3a) achieved smaller RMS velocity residuals than the least squares approach (described in section 3b). NM and least squares fits including shear outperformed the no shear fit using the same technique (Table 1). The fits with shear also displayed an increased number of Ekman-like spirals compared to the no shear case. This suggests that to properly isolate Ekman currents, accurate knowledge of the vertical structure of geostrophic currents in the Ekman layer is crucial. Fitted geostrophic shear did not differ significantly from the observed shear between 100 and 200 m.

b. *Ekman decay scales and eddy viscosities*

Mean Ekman layer depths and associated eddy viscosities (Table 2) were estimated over all profiles displaying decay scales of less than 1000 m and over a subset of profiles identified as displaying Ekman spirals (as defined in section 3a). The 95% confidence intervals were obtained from Eq. (9). Mean eddy viscosities ranged between $3.25 \pm 0.69 \times 10^{-2}$ (no shear, amplitude fit over Ekman-like spirals) and 0.447 ± 0.0932 m^2 s^{-1} (no shear, rotational fit over all data). These viscosities are consistent with prior studies in the Drake Passage

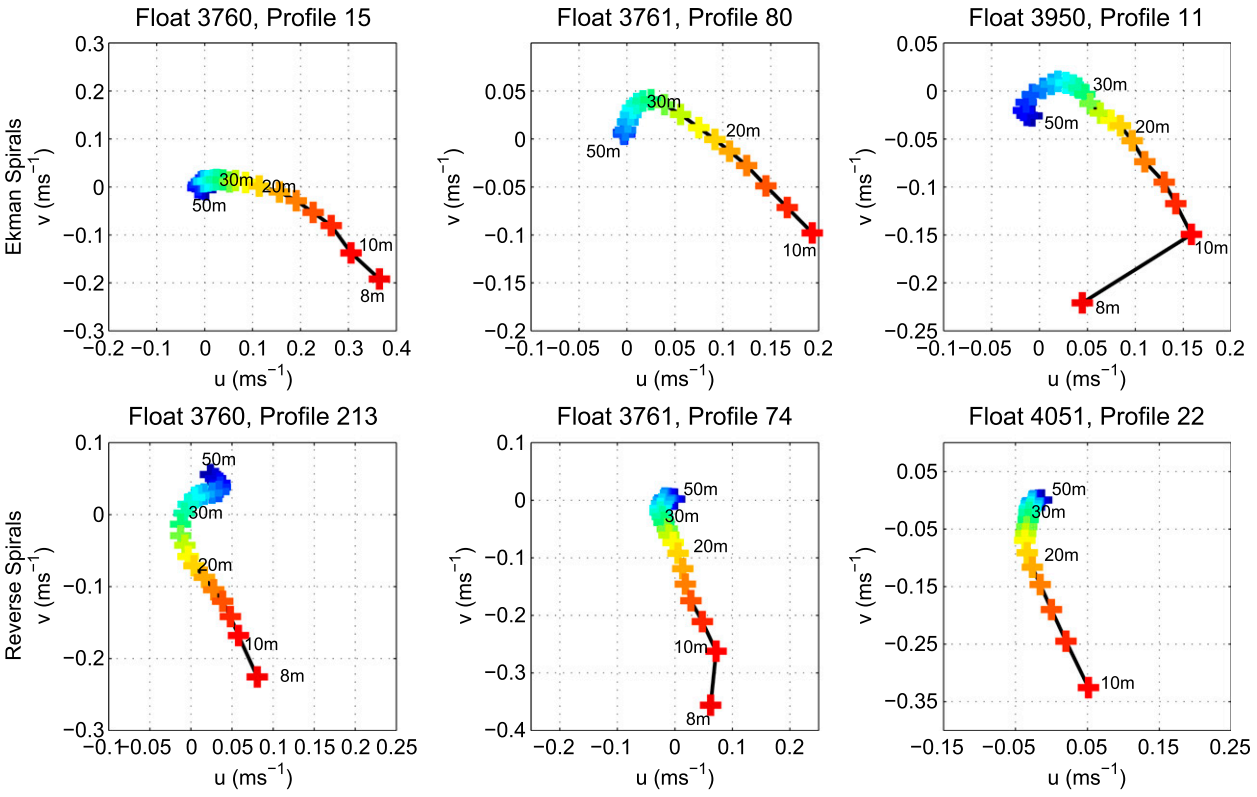

FIG. 4. Examples of individual EM-APEX float velocity profiles displaying (top) Ekman-like and (bottom) reversed spirals. Colors represent depths ranging from 8 (dark red) to 50 m (dark blue).

region; Lenn and Chereskin (2009) obtained viscosities between 3.08×10^{-2} and $22.10 \times 10^{-2}\,m^2\,s^{-1}$, while Polton et al. (2013) found viscosities of 8–12 $\times$ $10^{-2}\,m^2\,s^{-1}$.

Decay scales from all three fits (rotation, amplitude, and NM) were similar in the shear 1 and shear 2 cases (Table 2). However, in the no shear case there were statistically significant differences in mean decay scale between the rotational and amplitude fits. This difference in decay scales could indicate a compression of the Ekman spiral, as observed in several prior studies (Chereskin 1995; Lenn and Chereskin 2009; Price et al. 1987), such that amplitude decays faster than predicted. Investigating this further, we estimated the ratio of D_{rot} to D_{amp} from each profile, rather than the ratio of mean decay scales $\overline{D_{rot}}$ to $\overline{D_{amp}}$ presented in Table 2. The mean of D_{rot}/D_{amp} for the shear 1 case was 1.55 ± 0.16 for the Ekman-like spirals and 2.55 ± 0.30 for all profiles with decay scales of less than 1000 m. The ratios from the shear 2 case were similar to the shear 1 case. Corresponding values for the no shear case were 2.01 ± 0.26 and 3.38 ± 0.40, respectively. These values are broadly consistent with previous studies (Chereskin 1995; Lenn and Chereskin 2009; Price et al. 1987), which also found D_{rot} to be around 2 times larger than D_{amp}. It has been suggested (Price and Sundermeyer 1999; Price et al. 1987) that this compression of the Ekman spiral may be linked to stratification within the surface layers of the ocean. We explore this further in section 6.

5. Ekman transport

a. *Mean transport*

Time-mean profiles of Ekman transport from 200 to 14 m are shown in Fig. 6. Vectors of surface transport are shown in Fig. 7, assuming constant velocities between 14 m and the surface. The IFREMER reanalysis satellite winds and Eq. (9) were used to estimate the surface volume transport per unit pathlength for each profile.

Averaging these transports gave a mean surface transport of 1.22 ± 0.10 $m^2\,s^{-1}$. From integrating up the EM-APEX velocity data [Eq. (8)], we obtained mean transport magnitudes (Fig. 6, right; Fig. 7) between 200 m and the surface of 2.25 ± 0.71 $m^2\,s^{-1}$, 1.90 ± 0.72 $m^2\,s^{-1}$, and 2.86 ± 0.89 $m^2\,s^{-1}$ for the no shear, shear 1, and shear 2 cases, respectively. The no shear and shear 2 cases overestimated Ekman transport magnitude compared to wind-derived estimates from Eq. (9). The shear 1 case, while almost twice as large as the mean value of wind-derived

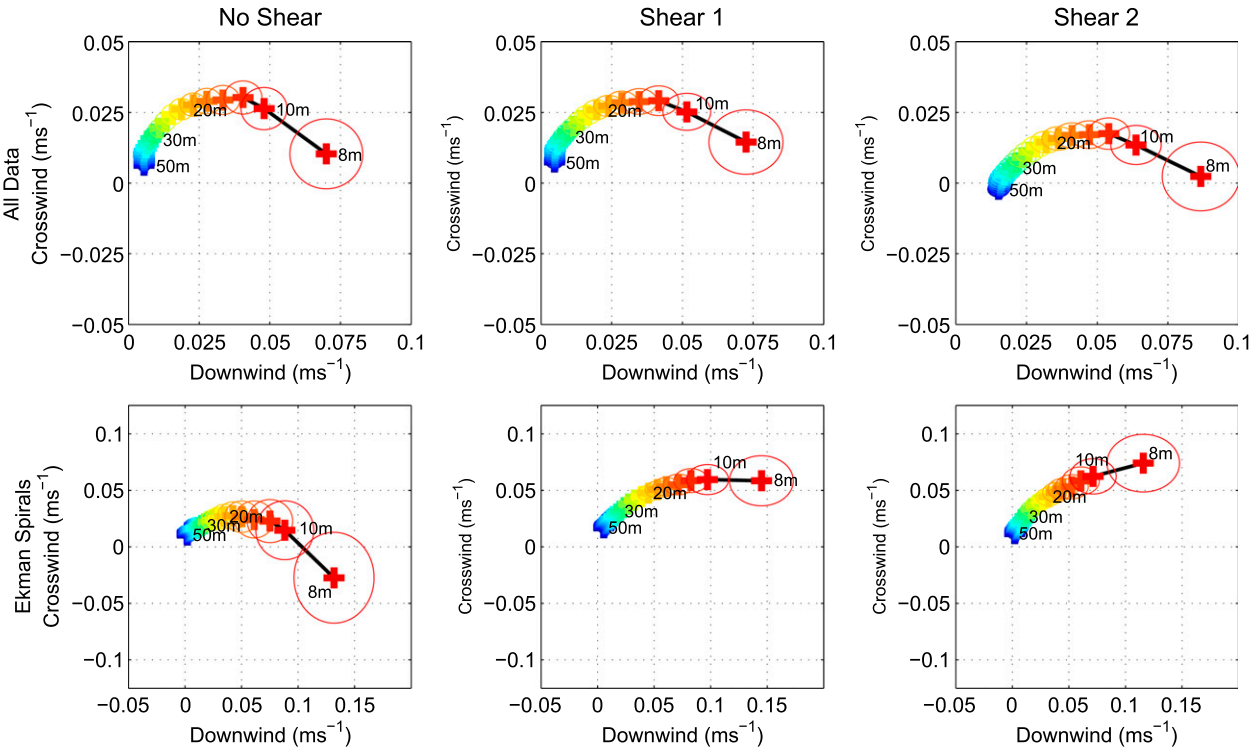

FIG. 5. (top) Observed Ekman spirals when averaged over all profiles and (bottom) all profiles displaying Ekman-like spirals. Colors represent depths ranging from 8 (dark red) to 50 m (dark blue). Ellipses represent 95% confidence intervals.

transport, still showed agreement at the 95% confidence level. The crosswind components of the no shear and shear 1 surface transport vectors (Fig. 7) also agreed with the wind-derived transport estimate.

Despite the general agreement in transport magnitude, the observed transport headings averaged over the profiles (Fig. 7) were closer to the wind than the theoretical expectation (90° to the left of the wind). In the no shear and shear 1 cases, the transport was 36° to the left of the wind, while the shear 2 case was skewed even farther downwind (5° to the right of the wind). Both shear cases displayed wider 95% confidence intervals than the no shear case. Confidence intervals were particularly wide in the downwind direction. Geostrophic currents (hence, shear) generally display similar heading to the time-mean winds. On the basis of these shear 2 results, we concluded that the fitting procedure applied in this case was inadequate, and we will not be discussing it further. For the rest of this paper any reference to the shear case will refer to the shear 1 fitting procedure.

The downwind skewing of mean transport is a significant difference from classical Ekman theory. To attempt to explain this difference, we considered the contributions from aliasing geostrophic shear, tidal flows, Stokes drift, the compression of Ekman spirals, and the transient response to time-varying wind forcing.

A possibility we were unable to investigate is that the downwind transport anomaly may be an artifact arising from the relatively short (around 2 months) period of high-resolution observations from the floats. Most prior in situ studies that successfully identified Ekman spirals have used time series of 5 months or greater duration. This possibility is supported by Lenn and Chereskin (2009) who found that observations matched theoretical transport in the multiyear average, but the same data averaged by season did not match the theoretical transport.

b. *Tides and transient winds*

Barotropic tidal velocities in the Kerguelen region from the TPXO7.2 model (Egbert and Erofeeva 2002) were on average three orders of magnitude smaller than the observed mean Ekman velocities. Furthermore, since barotropic tides are uniform through the water column, any barotropic flow would have been included in the reference velocity subtracted to isolate the ageostrophic flow. It is unlikely that barotropic tides explain the downwind transport anomaly. While baroclinic tides could contribute to the transport anomaly, we expect this effect to be weak. As discussed above, barotropic tides are weak while other studies (Müller 2013) indicate that the conversion from barotropic to baroclinic tidal energy in the Southern Ocean is small.

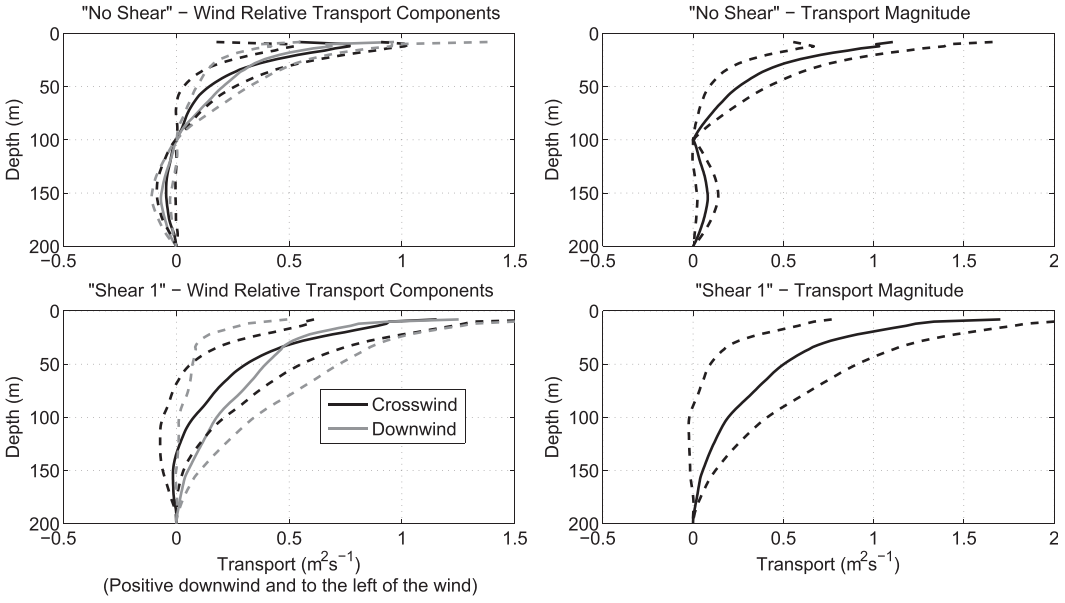

FIG. 6. Profiles of mean Ekman transport relative to 200 m for the (top) no shear and (bottom) shear 1. Solid, bold lines indicate the mean transport profiles; dashed lines indicate 95% confidence intervals. Transport is shown in (left) wind-relative component and (right) in magnitude.

Ekman dynamics are based upon a balance between frictional forces and Coriolis. Given forcing varying on time scales of less than a day this balance may be disrupted leading to modified current profiles and transport. We examined this possibility by taking a time 1D linear Ekman model consisting of a discrete time form of the momentum equation [Eq. (1)] and modifying the code to take time-varying input. Further details of the model can be found in Roach (2014). The models were then forced with winds interpolated along the trajectory of each float, assuming an eddy viscosity of $0.04\,\mathrm{m^2\,s^{-1}}$, with time steps of 40 s, a vertical resolution of 0.5 m, and a maximum depth of 1000 m. The resulting velocity data were filtered to suppress inertial oscillations as outlined in section 2a before transport was calculated. Time-mean modeled transport was in agreement with steady-state theory while time series of instantaneous transport magnitude and heading also demonstrated agreement between the model and steady-state theory. This result suggests that the observed transport anomaly cannot be attributed to the direct effects of low-frequency transient wind forcing.

c. *Compressed spirals and stratification*

Compression of Ekman spirals has previously been attributed to density stratification (Chereskin 1995; Price and Sundermeyer 1999; Price et al. 1987). We examined the effects of compressed mean spirals as a possible source of downwind component in the transport by considering independent decay scales for rotation and amplitude decay in the Ekman solution:

$$u_{\mathrm{ek}} + iv_{\mathrm{ek}} = V_{\mathrm{surf}} e^{z/D_{\mathrm{amp}}} e^{i(z/D_{\mathrm{rot}} + \pi/4)}. \qquad (12)$$

Synthetic spirals were created with decay scale ratios (D_{amp}:D_{rot}) between 1:0.25 and 1:5. The resulting wind-relative transport heading was calculated by integrating

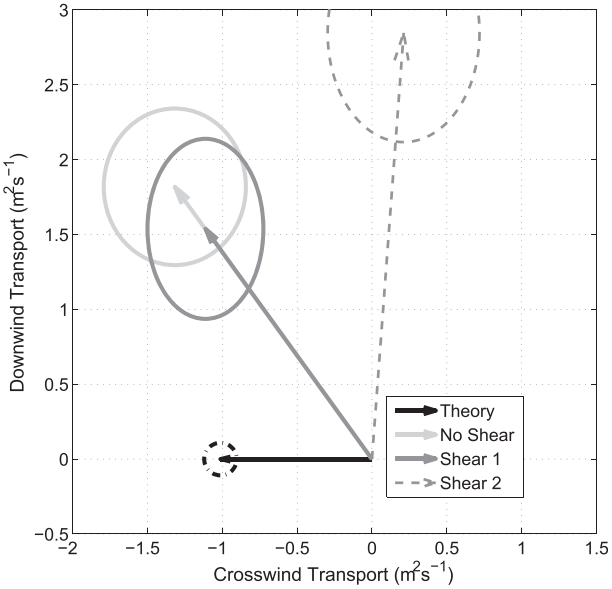

FIG. 7. Wind-relative vector plots of mean Ekman transport with 95% confidence intervals (ellipses). Blue line is the equilibrium Ekman transport from the interpolated wind stresses for each profile. Mean transport from the no shear (light gray) and shear 1 (dark gray) cases were skewed downwind by approximately 45°. The shear 2 case (black) was skewed farther downwind.

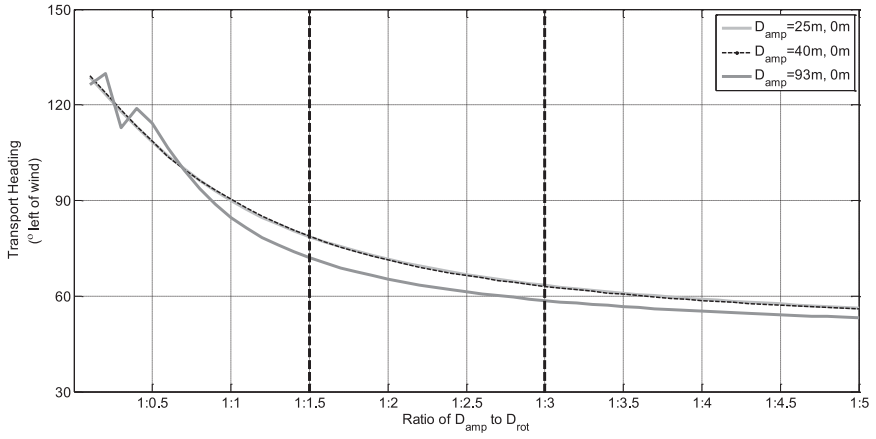

FIG. 8. Wind-relative transport heading computed from synthetic Ekman spirals of varying compression from (D_{amp}:D_{rot}) 1:0 to 1:5 for amplitude decay scales (D_{amp}) between 25 and 93 m. Vertical, thick, dashed lines indicate the typical range of compression seen in the data (1:1.5 to 1:3).

the computed velocities from 200 m to the surface (Fig. 8). Spirals displaying a level of compression comparable to that seen in our observations (between 1:1.5 and 1:3) displayed transport at the surface skewed between 88° and 68° left of the wind. These results suggest that a compressed Ekman spiral could account for a portion of the downwind transport anomaly seen in our observations.

d. Wave effects

Wave action can impact the Ekman layer by 1) enhancing turbulent mixing through direct wave actions such as wave breaking (Craig and Banner 1994); 2) causing a Stokes drift and creating a component of the flow parallel to the wave heading, which could enhance or reduce current speeds that we have diagnosed as Ekman currents; or 3) by direct coupling in the form of a Coriolis–Stokes forcing of the surface currents (Lewis and Belcher 2004; Polton et al. 2005).

Enhancement of turbulent mixing by wave action is typically confined to a layer within meters of the surface (Craig and Banner 1994), which is poorly sampled by the EM-APEX floats. Hence, wave-driven enhanced mixing lies beyond the scope of this paper.

To investigate the direct effect of Stokes drift on the observations, we assumed that only monochromatic deep-water waves were present. We calculated wave lengths from ERA-Interim data at the location and time of each EM-APEX profile using the deep-water dispersion relationship:

$$c_p = \sqrt{\frac{g\lambda}{2\pi}} = \frac{\lambda}{T_{\text{period}}},$$

$$\therefore \lambda = \frac{gT_{\text{period}}^2}{2\pi}, \tag{13}$$

where c_p denotes phase speed, g denotes the acceleration due to gravity (here taken as 9.81 $\text{m}^2\,\text{s}^{-1}$), T_{period} denotes wave period, and λ denotes wavelength.

Vertical profiles of Stokes drift velocities $\mathbf{u}_s$ (directed along wave headings obtained from ERA-Interim) were then computed as (Sutherland 2010)

$$|\mathbf{u}_s| \approx \sqrt{gl^3}A^2e^{2lz}, \tag{14}$$

where A denotes the wave amplitude (here taken as half the significant wave height) and l denotes the wavenumber ($2\pi/\lambda$).

Removal of Stokes drift from the estimated Ekman currents (assuming no geostrophic shear) reduced the downwind transport skewing in both the no shear and shear 1 cases (Fig. 9, center) but not enough to bring the transport heading into agreement with theory.

Stokes–Coriolis coupling is unlikely to have a significant effect on the observed transports because including the Stokes–Coriolis effect produces Eulerian currents that counteract the Lagrangian Stokes transport (McWilliams and Restrepo 1999; Polton et al. 2005). We examined the effect of Stokes–Coriolis coupling by applying the shallow wave forcing model proposed by Polton et al. (2005). This model assumes that the Stokes decay scale is much less than the Ekman decay scale, and so the net result of Stokes–Coriolis coupling can be represented by the standard Ekman balance [Eq. (1)] subject to a modified surface boundary stress incorporating the stress arising from Stokes drift:

$$\tau(z = 0\,\text{m}) = \boldsymbol{\tau}_0 - \rho\mathbf{f} \times \int_{-\infty}^{0} \mathbf{u}_s\, dz.$$

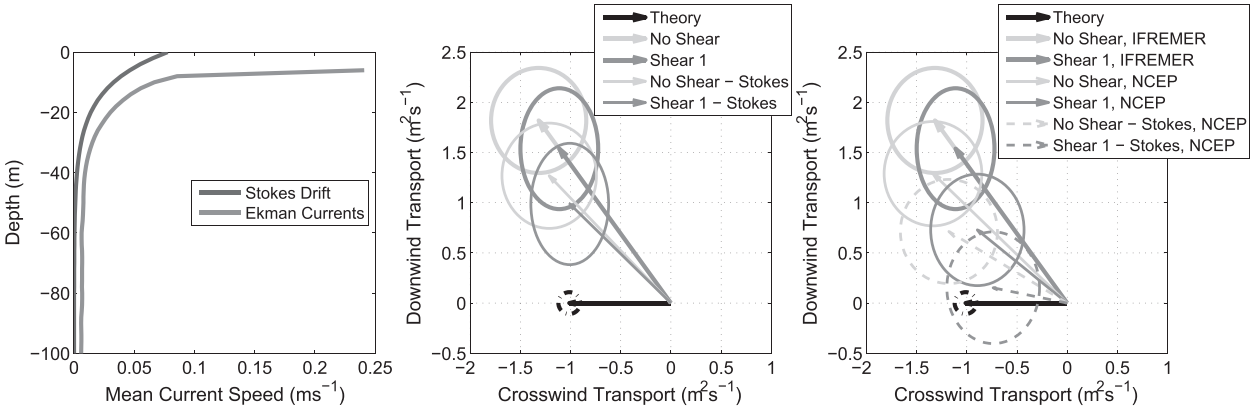

FIG. 9. (left) Example mean current speed profiles of Ekman currents and Stokes drift. (middle) Mean transport vectors at 14 m with and without Stokes drift explicitly removed from each velocity profile. (right) Mean transport vectors using IFREMER CERSAT (gray) and NCEP (black) winds. 95% confidence intervals are indicated by the ellipses.

Here, $\boldsymbol{\tau}_0$ is the surface wind stress vector. We then averaged transport in a reference frame based upon this modified surface stress instead of the wind stress. Surprisingly, this increased the downwind skewing rather than decreasing it. This suggests that Stokes–Coriolis coupling does not account for the downwind skewing transport observed in this study.

We conclude that with our data it is impractical to examine the effect of wave-enhanced turbulent mixing on the Ekman spiral. We found aliasing of Stokes drift cannot, in isolation, account for the downwind skewing of ageostrophic transport. Stokes–Coriolis coupling was found to increase the downwind transport anomaly; however, it must be noted that we considered here a simplified form of Stokes–Coriolis coupling.

e. Wind forcing dataset

In earlier sections, we used the IFREMER-blended satellite reanalysis wind fields. To test whether different wind products would produce the same results, we repeated the least squares fits for both the no shear and shear 1 cases using wind directions obtained from the NCEP–NCAR reanalysis.

Ekman decay scales and viscosities for the NCEP winds (not shown) did not differ significantly from the estimates obtained using IFREMER winds (section 4). Computing mean transport in a wind-relative coordinate frame with NCEP winds (Fig. 9, right) reduced the downwind transport anomaly but not enough to agree with theory within 95% confidence intervals. We subsequently superimposed the effect of aliasing Stokes drift and the change to NCEP winds to successfully bring the shear 1 mean transport into agreement with theory. This approach also reduced the skewing seen in the no shear case but not sufficiently to bring it into agreement with theory.

This evidence suggests we can explain the observed downwind transport anomaly as either a consequence of the compressed Ekman spirals or as a combination of our choice of wind fields and aliasing of Stokes drift into the Ekman spirals.

6. The effect of stratification on Ekman currents

Several previous theoretical and observational studies (Price and Sundermeyer 1999; Price et al. 1987) made the case that density stratification may have a significant impact on the structure of Ekman currents and transport. In our data, we have seen compression of the mean spirals, consistent with these previous studies. We therefore examine empirically the relationship between the structure of the Ekman currents and density stratification. The three properties we consider are the depth, strength, and stability of stratification.

The depth of stratification is taken to be the mixed layer depth. The strength of stratification is defined by the buoyancy frequency squared N^2. The gradient Richardson number (Stewart 2008) is used to define the stability of the stratification:

$$\mathrm{Ri} = \frac{N^2}{(\partial U/\partial z)^2}. \tag{15}$$

Buoyancy frequencies and gradient Richardson numbers were calculated from observed densities and Ekman velocity shear on a vertical grid of 2 m.

The bulk Richardson number Ri_b, computed across the mixed layer interface, was used to define the stability of the mixed layer (Price et al. 1986):

$$\mathrm{Ri}_b = \frac{g\Delta\rho h}{\rho_0(\Delta u)^2}. \tag{16}$$

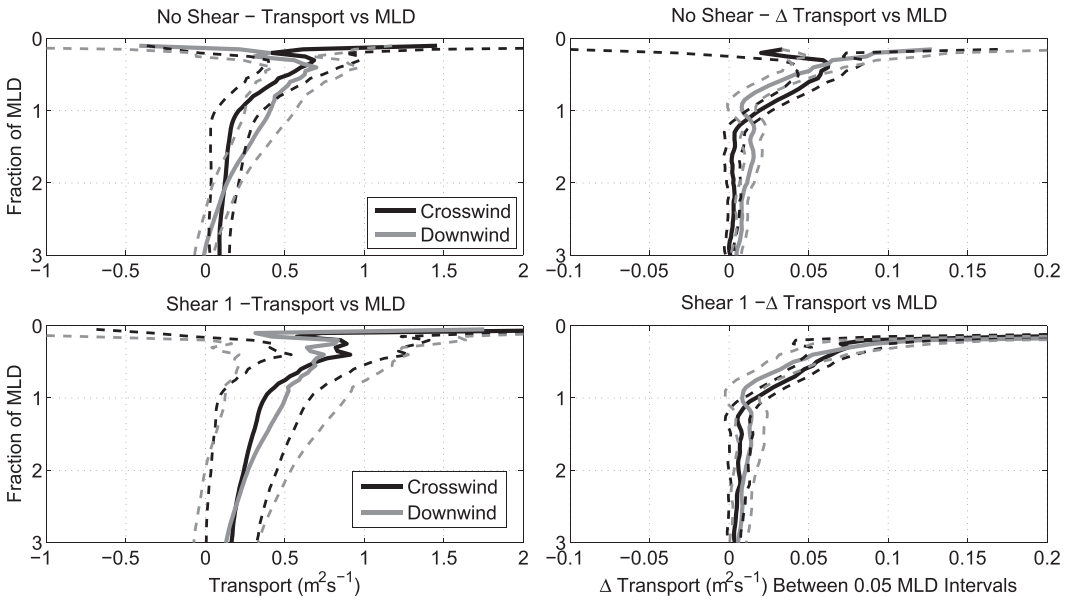

FIG. 10. (left) Profiles of Ekman transport and (right) the difference in Ekman transport between 0.05 MLD intervals as functions of MLD for both the (top) no shear case and (bottom) shear 1 case. Solid lines indicate the mean profiles while dashed lines indicate 95% confidence intervals.

Here, g denotes the acceleration due to gravity; h denotes the mixed layer depth; $\Delta\rho$ is the density difference between the mixed layer and just below the mixed layer; Δu is the difference in total velocity across the base of the mixed layer; and ρ_0 is the surface reference density. A bulk Richardson number of less than 0.65 implies the mixed layer is unstable and will tend to entrain additional water into the mixed layer.

a. Depth and strength of stratification

Mixed layer depth (section 3c) from the EM-APEX profiles varied between 7 and 330 m, with a mean of 43.8 m and a standard deviation of 25.2 m. Profiles of mean MLD-normalized transport (section 3c) for both the no shear and shear 1 cases are shown in the left-hand column of Fig. 10. The vertical gradients of transport, calculated as the first difference between adjacent mixed layer depth fractions, are shown in the right-hand column of Fig. 10.

Transport was surface intensified with over half the transport occurring above the mixed layer (Fig. 10, left). This behavior is potentially indicative of coupling between Ekman spiral structure and stratification. The surface intensification of transport within the mixed layer (Fig. 10, right) is not consistent with slablike behavior identified at lower latitudes in a number of previous studies (McNally 1981; Wijffels et al. 1994). This intensification raises the potential for second-order errors in the transports of heat and freshwater by the Ekman layer in these studies.

Plots of Ri and N^2 for two profiles are shown in Fig. 11. Stratification was generally statically stable ($N^2 > 0$) over the entire depth range. Above the thermocline (defined by the maximum N^2 within the upper 200 m), the gradient Richardson numbers were typically smaller [$O(10^{-3}$ to 1)] than in the interior [O(1 to 100)]. This tendency for lower Ri near the surface is expected since both Ekman and Stokes shears are surface intensified.

Dynamical instability (occurring when Ri < 0.25) was rare below the thermocline, and when observed it was confined to small vertical scales (2–4 m). Above the thermocline, sustained dynamical instability was found on vertical scales of 10–70 m; examination of individual profiles suggested a linkage between the onset of instability and mixed layer depth. This was reinforced when we plotted the maximum depth of ''sustained'' instability (here taken as two or more data points with Ri < 0.25 within a 10-m depth range) against MLD (Fig. 12). Almost all cases of instability occurred at depths equal to or less than the MLD. The maximum depth of sustained dynamic instability displayed no relationship to the observed Ekman decay scales.

We examined the relationship between stratification and the vertical structure of Ekman currents by considering correlations between the magnitude ($\log_{10}$) of the observed decay scales and parameters including MLD, thermocline depth, density difference across the base of the mixed layer, maximum Richardson number, and maximum N^2. We were unable to identify any

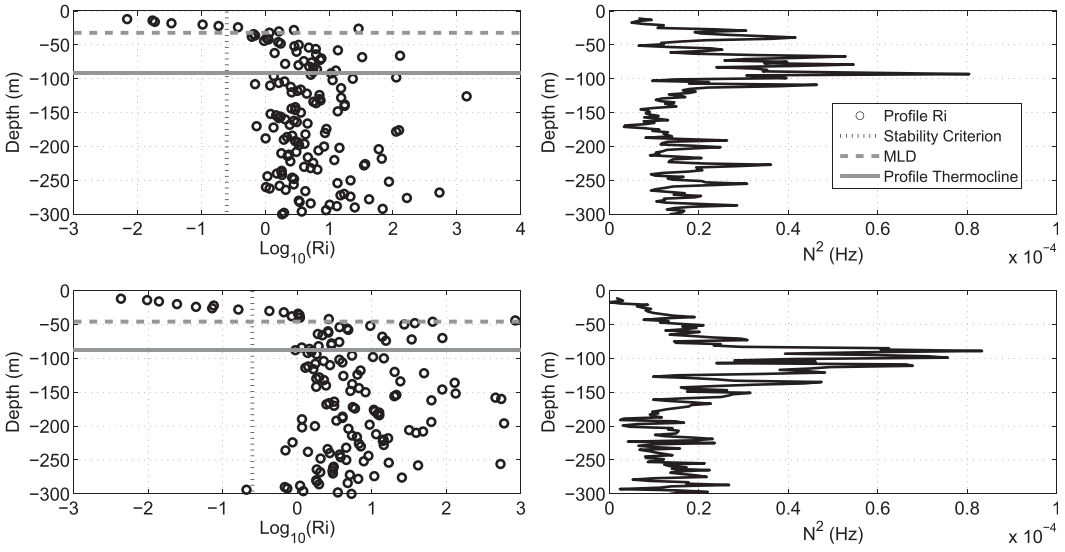

FIG. 11. Profiles of (left) Ri and (right) N^2 for (top) float 3760 profile 42 and (bottom) float 3761 profile 80. The standard criterion for dynamic instability (Ri < 0.25) is indicated by the vertical dashed line; MLD and thermocline depth are indicated by the horizontal solid and dashed lines. Note that in both cases instability (Ri < 0.25) was principally confined to the mixed layer.

statistically significant relationships between these parameters and Ekman decay scales.

We found statistically significant but weak correlations (0.58 for D_{amp} and 0.17 for D_{rot}) between decay scales and the bulk Richardson number (Fig. 13). This correlation implies Ekman decay scales were larger when the mixed layer was more stable. The correlation between bulk Richardson numbers and decay scales may seem counterintuitive; however, it is actually perfectly logical. The bulk Richardson number is a competition between the density gradient and shear across the mixed layer depth [Eq. (16)]. We have defined the mixed layer depth in terms of a constant density difference (section 3c), leaving the shear across the mixed layer as the only active element in setting Ri_b. For given surface stress and background geostrophic shear, a deeper Ekman decay scale (higher viscosity) implies a lower shear than a shallow Ekman decay scale. Since Ri_b is inversely proportional to the shear, a large decay scale would result in a high Ri_b. Thus, Fig. 13 is showing a consistent relationship of mixed layer with higher viscosity when it is more stable (corresponding to higher Ri_b).

b. Local eddy viscosities

Mean eddy viscosity profiles calculated as described in section 3d (Fig. 14, left) were of similar magnitude, if somewhat weaker, than comparable observations in the Drake Passage (Lenn and Chereskin 2009). There was a tendency for greater viscosities to be observed closer to the surface and for the shear case to produce larger viscosities than the no shear case. When considering the viscosity profiles with the vertical coordinate as a proportion of MLD (Fig. 14, center and right), the no shear viscosity profile displayed a distinct trend for viscosity to decrease with increasing depth. Viscosity decreases approximately exponentially from around $10^{-2}\,\mathrm{m^2\,s^{-1}}$ near the surface to 2–3 $\times\ 10^{-3}\,\mathrm{m^2\,s^{-1}}$ at a depth of 2–3 times the MLD.

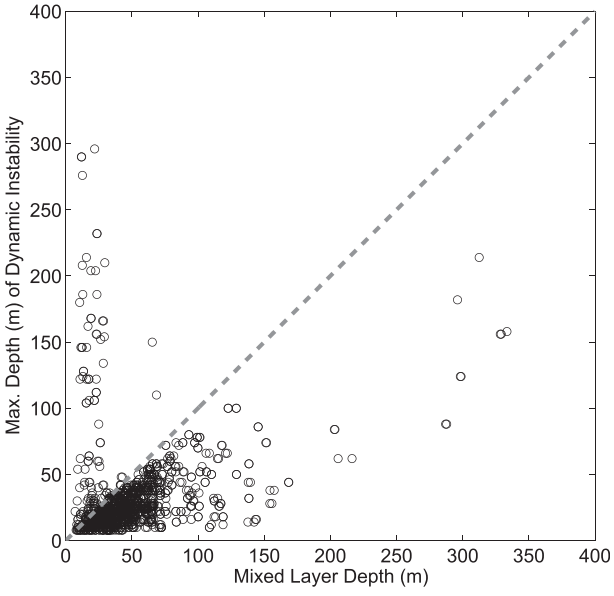

FIG. 12. Maximum depth of sustained dynamic instability plotted against mixed layer depth. The dashed gray line corresponds to a 1:1 ratio between the depth of instability and the mixed layer depth.

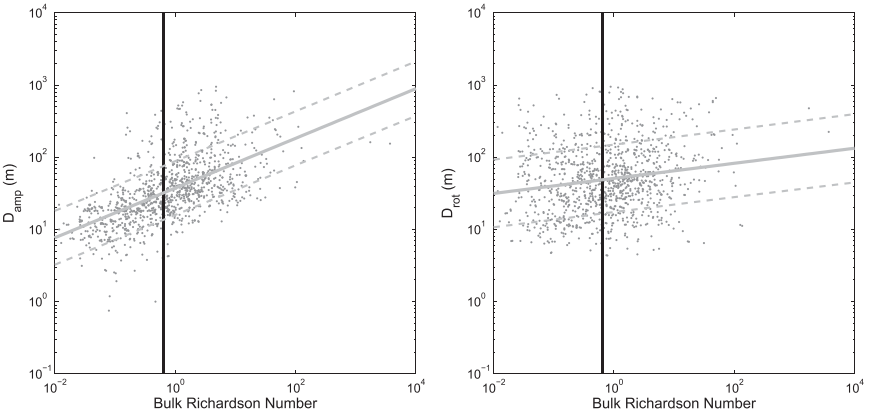

FIG. 13. Ekman decay scales vs bulk Richardson numbers Ri_b for decay scales estimated from (left) current amplitude and (right) current rotation. Solid red and blue lines represent logarithmic fits to the data; dashed lines indicate confidence intervals estimated from the MATLAB polyfit routine. The vertical black line indicates the critical value of Ri_b (0.65).

The viscosity profile for the shear case is more consistent; over the 0–3 MLD range the viscosity is generally around 1–3 $\times$ $10^{-2}\,\mathrm{m^2\,s^{-1}}$. However, there is still some tendency for smaller viscosities to occur below the mixed layer.

To properly test whether viscosity could be treated as constant with depth, we considered how the viscosity varied and the related uncertainty over a range of depths. We divided the no shear and shear case mean viscosity profiles into three subsets: all data between 0.3 and 5 MLD (denoted all data), data between 0.3 and 1 MLD (denoted mixed layer), and data between 1.5 and 3 MLD (denoted deep). We excluded data shallower than 0.3 MLD as much of that data would come from depths only poorly sampled by the EM-APEX floats. Linear fits (not shown) were applied to each depth range of the viscosity profiles and the resulting fits and 95% confidence intervals plotted. Exponential fits (Fig. 13, center and right) were applied by using a linear fit to profiles of $\log_{10}[k(z)]$. The MLD-normalized viscosity profiles (Fig. 13, center and right) suggested that either linear or exponential fits provide the best match to the mean current profiles.

Initial examination of the mean values of the mixed layer and deep fits suggested viscosity values were sensitive to the depth range. However, considering confidence intervals, it was not possible to distinguish between any of the mixed layer fits and the corresponding "all data" fits over the 0.3 to 1 MLD interval. Similarly, over the 1.5 to 3 MLD interval, there was no significant difference between the "deep" fits and the all data fits.

We examined the fits to see if it was possible to reconcile them to a constant viscosity. No such viscosities could be identified for the linear no shear fits, but a constant viscosity between 3.76 $\times$ 10^{-3} and 4.83 $\times$ $10^{-3}\,\mathrm{m^2\,s^{-1}}$ satisfied the confidence intervals for the exponential fits. Examining all fits for the shear 1 viscosity profile in a similar manner indicated a constant viscosity between 1.37 $\times$ 10^{-2} and 1.60 $\times$ $10^{-2}\,\mathrm{m^2\,s^{-1}}$ satisfied the confidence intervals for the linear fits and a constant viscosity between 1.14 $\times$ 10^{-2} and 1.53 $\times$ $10^{-2}\,\mathrm{m^2\,s^{-1}}$ satisfied the confidence intervals for the exponential fits.

Hence, there is no statistical difference between these three empirical viscosity models for the water column, and using the "Occam's razor" approach, we conclude that only a constant viscosity model is required to explain the available observations.

7. Discussion and conclusions

We have detected and characterized Ekman spirals for the first time using EM-APEX velocity profiling floats in the Southern Ocean. In addition to identifying individual profiles displaying spirals consistent with time-mean Ekman theory, we also identified profiles showing spirals with reversed rotation with depth. Our tests have shown that these reversed spirals are consistent with solutions of the Ekman balance [Eq. (1)] for high frequency or rapid cyclonic wind forcing, suggesting that it is necessary to resolve time-varying Ekman currents. We will visit time-varying spirals further in subsequent papers Roach et al. (2015, manuscript submitted to *J. Phys. Oceanogr.*).

Eddy viscosities ranged between 3.2 $\times$ 10^{-2} and 44.7 $\times$ $10^{-2}\,\mathrm{m^2\,s^{-1}}$ (corresponding to decay scales of 25 and 93 m), in general agreement with previous studies in the Drake Passage (Lenn and Chereskin 2009; Polton et al. 2013). When we assumed a constant geostrophic velocity within the Ekman layer, mean viscosities and decay scales obtained from the rotational least squares fit were larger than those obtained from the current

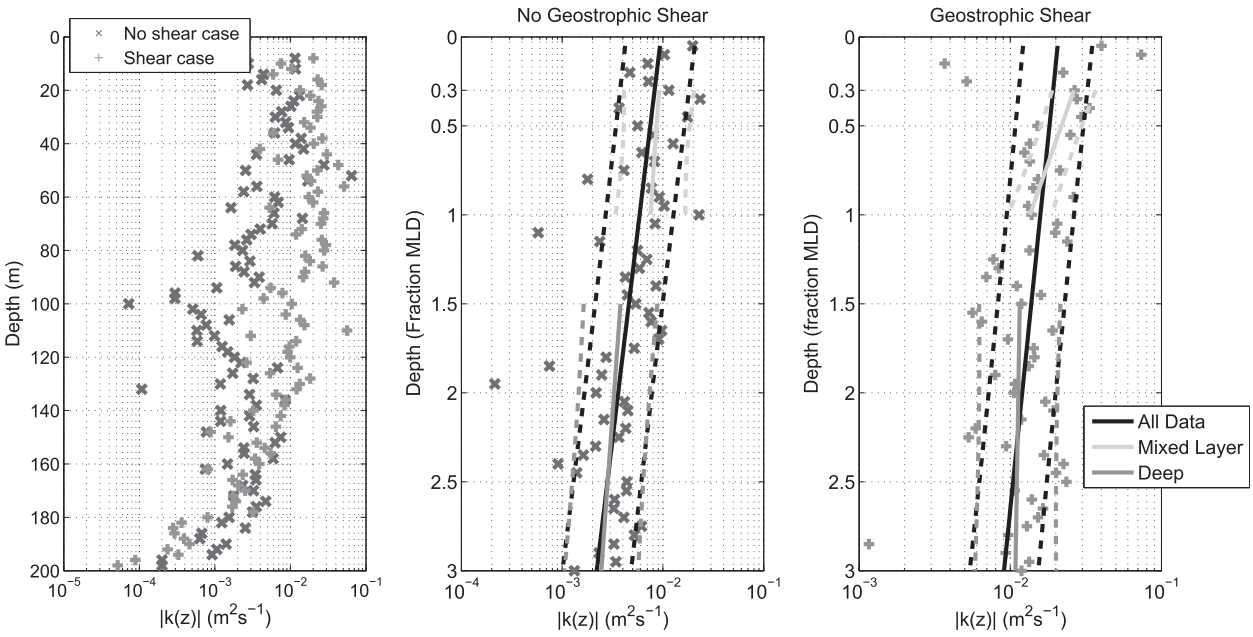

FIG. 14. (left) Mean viscosity amplitude profiles by depth. Mean viscosity profiles [(middle) no shear and (right) shear] as a function of fraction of MLD. Exponential fits to viscosities in the mixed layer, ocean interior, and over the entire profile are shown.

amplitude least squares fit, resulting in compressed spirals, as found in Polton et al. (2013). Several other studies also found compression in observations of open-ocean Ekman spirals (Chereskin 1995; Lenn and Chereskin 2009; Price et al. 1987). If we assumed a constant geostrophic shear within the Ekman layer, as in Polton et al. (2013), both least squares fits (rotation and amplitude decay) produced mean viscosities more consistent with each other. Moreover, the compression of the spirals (computed on a float by float basis) decreased, with the ratio between the rotational and amplitude decay scales becoming closer to 1:1. Fits with geostrophic shear also showed more individual profiles displaying Ekman-like spirals and decreased RMS residuals. As a consequence, we believe that the best estimates of the eddy viscosity is actually in the narrower range of 5×10^{-2} and $25 \times 10^{-2}\,\mathrm{m^2\,s^{-1}}$ based on the shear 1 estimates (Table 2). This suggests that using fitting procedures capable of using the vectorial nature of the data offers significant advantages over the traditional approach of fitting by either current amplitude or heading.

This convergence in decay scales from the two methods of estimation indicates that the vertical structure of the geostrophic currents must be explicitly resolved to properly isolate Ekman currents. This suggests that the compressed spirals previously seen in previous studies are, in the Southern Ocean context of deep and weakly stratified mixed layers, principally an artifact of assuming a constant geostrophic current. Our conclusion based on EM-APEX data at the northern Kerguelen Plateau agrees with the conclusion of Polton et al. (2013) using long records of shipboard ADCP across the Drake Passage, demonstrating that this is a robust result that is likely representative of the entire Southern Ocean. It also raises questions if geostrophic shear could also explain compressed Ekman spirals observed at lower latitudes (Price and Sundermeyer 1999; Price et al. 1987) that have previously been attributed to "surface trapping" driven by diurnal cycles of stratification. Further observations and analysis are required to increase the "signal to noise" in order to reveal the effect of stratification in Southern Ocean waters on surface Ekman currents and to examine the effect of geostrophic shear on Ekman currents at lower latitude.

Mean viscosity profiles as a function of MLD-normalized depth suggested either linear or exponential decay of viscosity with increasing depth. However, we subsequently determined it was also possible to reconcile these observations within confidence intervals to a constant eddy viscosity.

Mean observed transport magnitude was found to be consistent with that expected from wind data and steady-state Ekman theory. However, the ageostrophic transport heading was skewed downwind compared to classical Ekman theory. This transport anomaly proved surprisingly robust to the selection of profiles. Low-frequency transient wind forcing and inclusion of systematic residual geostrophic currents when integrating the Ekman transport had little effect on the downwind transport anomaly. We also examined the effect of

Stokes drift and Stokes–Coriolis coupling on the transport skewing; explicitly removing Stokes drift from each ageostrophic profile reduced the downwind anomaly and when combined with use of NCEP winds, rather than IFREMER winds, brought observed and theoretical time-mean transport into agreement. Stokes–Coriolis coupling was found to exacerbate the downwind transport anomaly; however, it must be noted that we considered Stokes–Coriolis coupling in a simplified manner. It is possible the transport anomaly could arise from the compression seen in the Ekman spirals, but a more likely explanation is discrepancies between reanalysis and (unobserved) in situ winds combined with aliasing of Stokes drift.

Finally, we examined the possible relationship between stratification and Ekman currents from a variety of angles. Ekman transport and dynamic instability were largely confined to the mixed layer. While superficially suggestive of the surface trapping of the Ekman currents by density stratification, this association is likely coincidental as the mean mixed layer depth and Ekman decay scales are often comparable in magnitude. We found a weak relationship between Ekman decay scales and bulk Richardson numbers, implying that decay scales tended to be larger when the mixed layer was stable. We found no other significant relationships between stratification and observed Ekman decay scales. We conclude that stratification across the Ekman layer does not affect Ekman currents in the Antarctic Circumpolar Current. This contradicts the results of Price et al. (1987) and Price and Sundermeyer (1999) likely because of the intrinsic difference between the stratified tropical and subtropical waters examined in their study and the weakly stratified, deep mixed layers in the Southern Ocean examined in our study.

Our results from 2 months (1400 profiles) of EM-APEX data in the Antarctic Circumpolar Current at the northern Kerguelen Plateau reinforce the results of Polton et al. (2013) from long-term shipboard ADCP transects across the Drake Passage. That is, provided geostrophic shear is accounted for, a constant viscosity Ekman model adequately represents wind-driven currents in the Southern Ocean surface layers. The agreement between our two studies, in different parts of the Southern Ocean, indicates that this result is robust and likely representative of the response of the upper ocean to winds across the entire Southern Ocean. It is remarkable that the simple linear theory proposed by Ekman in 1905 stands up to the test of modern, high-resolution observations of Ekman currents.

Acknowledgments. We thank the scientists and crew involved in the Southern Ocean FINE-structure project. We thank Yueng Lenn and Shane Elipot for valuable discussions. We also thank the three reviewers whose comments improved this paper. C. J. R. was supported by the CSIRO-University of Tasmania Quantitative Marine Science programme and the CSIRO Office of the Chief Executive Postgraduate Scholarship. Funding for the Australian contribution to SOFINE was provided by the Australian Research Council (DP0877098) and the Antarctic Science Program (Projects 3002 and 3228).

REFERENCES

Bentamy, A., D. Croize-Fillon, P. Queffeulou, C. Liu, and H. Roquet, 2009: Evaluation of high-resolution surface wind products at global and regional scales. *J. Oper. Oceanogr.,* **2,** 15–27.

Chereskin, T. K., 1995: Direct evidence for an Ekman balance in the California Current. *J. Geophys. Res.,* **100,** 18 261–18 269, doi:10.1029/95JC02182.

——, and D. Roemmich, 1991: A comparison of measured and wind-derived Ekman transport at 11°N in the Atlantic Ocean. *J. Phys. Oceanogr.,* **21,** 869–878, doi:10.1175/1520-0485(1991)021<0869:ACOMAW>2.0.CO;2.

Craig, P. D., and M. L. Banner, 1994: Modeling wave-enhanced turbulence in the ocean surface layer. *J. Phys. Oceanogr.,* **24,** 2546–2559, doi:10.1175/1520-0485(1994)024<2546:MWETIT>2.0.CO;2.

Egbert, G. D., and S. Y. Erofeeva, 2002: Efficient inverse modeling of barotropic ocean tides. *J. Atmos. Oceanic Technol.,* **19,** 183–204, doi:10.1175/1520-0426(2002)019<0183:EIMOBO>2.0.CO;2.

Ekman, V. W., 1905: On the influence of the Earth's rotation on ocean currents. *Ark. Mat., Astron. Fys.,* **2,** 1–52.

Elipot, S., and S. T. Gille, 2009: Ekman layers in the Southern Ocean: Spectral models and observations, vertical viscosity and boundary layer depth. *Ocean Sci.,* **5,** 115–139, doi:10.5194/os-5-115-2009.

Halpern, D., 1974: Observations of the deepening of the wind-mixed layer in the northeast Pacific Ocean. *J. Phys. Oceanogr.,* **4,** 454–466, doi:10.1175/1520-0485(1974)004<0454:OOTDOT>2.0.CO;2.

Hasselmann, S., and Coauthors, 1988: The WAM model—A third generation ocean wave prediction model. *J. Phys. Oceanogr.,* **18,** 1775–1810, doi:10.1175/1520-0485(1988)018<1775:TWMTGO>2.0.CO;2.

Hunkins, K., 1966: Ekman drift currents in the Arctic Ocean. *Deep-Sea Res. Oceanogr. Abstr.,* **13,** 607–620, doi:10.1016/0011-7471(66)90592-4.

Lenn, Y., and T. K. Chereskin, 2009: Observation of Ekman currents in the Southern Ocean. *J. Phys. Oceanogr.,* **39,** 768–779, doi:10.1175/2008JPO3943.1.

Lewis, D. M., and S. E. Belcher, 2004: Time-dependent, coupled, Ekman boundary layer solutions incorporating Stokes drift. *Dyn. Atmos. Oceans,* **37,** 313–351, doi:10.1016/j.dynatmoce.2003.11.001.

McNally, G. J., 1981: Satellite-tracked drift buoy observations of the near-surface flow in the eastern mid-latitude North Pacific. *J. Geophys. Res.,* **86,** 8022–8030, doi:10.1029/JC086iC09p08022.

McWilliams, J. C., and J. M. Restrepo, 1999: The wave-driven ocean circulation. *J. Phys. Oceanogr.,* **29,** 2523–2540, doi:10.1175/1520-0485(1999)029<2523:TWDOC>2.0.CO;2.

Meyer, A., B. M. Sloyan, K. L. Polzin, H. E. Phillips, and N. L. Bindoff, 2015: Mixing variability in the Southern Ocean. *J. Phys. Oceanogr.,* **45,** 966–987, doi:10.1175/JPO-D-14-0110.1.

Müller, M., 2013: On the space- and time-dependence of barotropic-to-baroclinic tidal energy conversion. *Ocean Modell.,* **72,** 242–252, doi:10.1016/j.ocemod.2013.09.007.

Naveira Garabato, A., N. L. Bindoff, H. E. Phillips, K. L. Polzin, B. Sloyan, D. Stevens, and S. Waterman, 2009: RRS *James Cook* cruise 29, 01 Nov-22 Dec 2008: SOFine cruise report: Southern Ocean finestructure. National Oceanography Centre Southampton Cruise Rep. 35, 216 pp.

Nelder, J. A., and R. Mead, 1965: A simplex method for function minimization. *Comput. J.,* **7,** 308–313, doi:10.1093/comjnl/7.4.308.

Persson, A., and F. Grazzini, 2007: User guide to ECMWF forecast products. Meteorological Bull. M3.2, 153 pp. [Available online at www.uio.no/studier/emner/matnat/geofag/GEF4220/v09/undervisningsmateriale/Persson_user_guide.pdf.]

Phillips, H. E., and N. L. Bindoff, 2014: On the nonequivalent barotropic structure of the Antarctic Circumpolar Current: An observational perspective. *J. Geophys. Res. Oceans,* **119,** 5221–5243, doi:10.1002/2013JC009516.

Polton, J. A., D. M. Lewis, and S. E. Belcher, 2005: The role of wave-induced Coriolis–Stokes forcing on the wind-driven mixed layer. *J. Phys. Oceanogr.,* **35,** 444–457, doi:10.1175/JPO2701.1.

——, Y. Lenn, S. Elipot, T. K. Chereskin, and J. Sprintall, 2013: Can Drake Passage observations match Ekman's classic theory. *J. Phys. Oceanogr.,* **43,** 1733–1740, doi:10.1175/JPO-D-13-034.1.

Price, J. F., and M. A. Sundermeyer, 1999: Stratified Ekman layers. *J. Geophys. Res.,* **104,** 20 467–20 494, doi:10.1029/1999JC900164.

——, R. A. Weller, and R. Pinkel, 1986: Diurnal cycling: Observations and models of the upper ocean response to diurnal heating, cooling and wind mixing. *J. Geophys. Res.,* **91,** 8411–8427, doi:10.1029/JC091iC07p08411.

——, ——, and R. R. Schudlich, 1987: Wind-driven ocean currents and Ekman transport. *Science,* **238,** 1534–1538, doi:10.1126/science.238.4833.1534.

Roach, C. J., 2014: Ekman currents in the Antarctic Circumpolar Current. Ph.D. thesis, Institute for Marine and Antarctic Studies, University of Tasmania, 233 pp. [Available online at http://eprints.utas.edu.au/22416/.]

Rudnick, D. L., and R. A. Weller, 1993: Observations of superinertial and near-inertial wind-driven flow. *J. Phys. Oceanogr.,* **23,** 2351–2359, doi:10.1175/1520-0485(1993)023<2351:OOSANI>2.0.CO;2.

Sallée, J.-B., N. Wienders, K. Speer, and R. Morrow, 2006: Formation of subantarctic mode water in the southeastern Indian Ocean. *Ocean Dyn.,* **56,** 525–542, doi:10.1007/s10236-005-0054-x.

Sanford, T. B., R. G. Drever, and J. H. Dunlap, 1978: A velocity profiler based on the principles of geomagnetic induction. *Deep-Sea Res.,* **25,** 183–210, doi:10.1016/0146-6291(78)90006-1.

——, J. H. Dunlap, J. A. Carlson, D. C. Webb, and J. B. Girton, 2005: Autonomous velocity and density profiler: EM-APEX. *Proc. IEEE/OES Eighth Working Conf. on Current Measurement Technology,* Southampton, United Kingdom, IEEE, 152–156, doi:10.1109/CCM.2005.1506361.

——, J. F. Price, and J. B. Girton, 2011: Upper-ocean response to Hurricane Frances (2004) observed by profiling EM-APEX floats. *J. Phys. Oceanogr.,* **41,** 1041–1056, doi:10.1175/2010JPO4313.1.

Schudlich, R. R., and J. F. Price, 1998: Observations of seasonal variation in the Ekman layer. *J. Phys. Oceanogr.,* **28,** 1187–1204, doi:10.1175/1520-0485(1998)028<1187:OOSVIT>2.0.CO;2.

Smith, W. H. F., and D. T. Sandwell, 1997: Global sea floor topography from satellite and ship depth soundings. *Science,* **277,** 1957–1962, doi:10.1126/science.277.5334.1956.

Speer, K., S. R. Rintoul, and B. Sloyan, 2000: The diabatic Deacon cell. *J. Phys. Oceanogr.,* **30,** 3212–3222, doi:10.1175/1520-0485(2000)030<3212:TDDC>2.0.CO;2.

Stewart, R. H., 2008: Introduction to physical oceanography. Department of Oceanography, Texas A&M University. [Available online at http://oceanworld.tamu.edu/resources/ocng_textbook/contents.html.]

Sutherland, B. R., 2010: *Internal Gravity Waves.* Cambridge University Press, 377 pp.

Wijffels, S., E. Firing, and H. Bryden, 1994: Direct observation of the Ekman balance at 10°N in the Pacific. *J. Phys. Oceanogr.,* **24,** 1666–1679, doi:10.1175/1520-0485(1994)024<1666:DOOTEB>2.0.CO;2.

Yelland, M., and P. K. Taylor, 1996: Wind stress measurements from the open ocean. *J. Phys. Oceanogr.,* **26,** 541–558, doi:10.1175/1520-0485(1996)026<0541:WSMFTO>2.0.CO;2.